Full length article

Programmable spectral phase coding of an amplified spontaneous emission light source

Lei Wang [a,*], A.M. Weiner [b,1]

[a] *Department of Physics, Purdue University, W. Lafayette, IN 47907, USA*
[b] *School of Electrical and Computer Engineering, Purdue University, W. Lafayette, IN 47907, USA*

Abstract

The use of a programmable pulse shaper for spectral phase coding of broadband incoherent light is discussed. Our experiments result in tailoring of the electric field cross-correlation function between the shaped and the original unshaped light. This technique is illustrated through several examples, including binary spectral phase filtering, gray-level spectral phase filtering using quadratic-residue codes, generation of coherence functions consisting of trains of coherence peaks via periodic gray-level phase coding, and dispersion compensation for broadband incoherent light. Spectral interferometry measurements of phase coded incoherent light are also presented. Based upon careful alignment of the pulse shaper, we were able to obtain excellent agreement between the experiments and theoretical simulations. In some cases we found that the usual assumption of a linear spectral dispersion at the masking plane of the pulse shaper led to distortion in the shaped correlation functions. Here we demonstrate the ability to measure the exact spectral dispersion, which is then taken into account when programming the spectral phase modulation. This removes the observed distortion, leading once again to excellent agreement between theory and experiment. © 1999 Elsevier Science B.V. All rights reserved.

Keywords: Pulse shaper; Liquid crystal modulator; Spectral coding; Coherence coding; Optical communication; Dispersion compensation

1. Introduction

Spectral slicing of incoherent broadband light sources, such as light-emitting diodes, superluminescent diodes and erbium-doped fiber amplifiers (EDFAs), has received significant attention for wavelength division multiplexing applications due to the simplicity and low cost of these sources [1,2]. Inco-herent light sources are also candidates for optical code-division multiple-access (CDMA) network applications due to their simplicity and broad bandwidth [3,4]. Several approaches have been proposed for CDMA based on incoherent light sources. The most promising of these depends on coherent processing of the incoherent light signal, meaning that coding and decoding are based on manipulation of the optical fields rather than just the intensities. For a review see Ref. [5]. Proposed schemes include spectral amplitude coding [6,7], coherence multiplexing [8,9] and coherence coding [4,10]. In the case of coherence coding, a pseudorandom phase code is

---
* Corresponding author. Tel.: +1-765-496-3201; fax: +1-765-494-6951; e-mail: wlei@ecn.purdue.edu
[1] Tel.: +1-765-494-5574; e-mail: amw@ecn.purdue.edu

impressed onto the optical spectrum, resulting in manipulation of the temporal coherence function.

Binary spectral phase coding of incoherent light was first demonstrated by using visible light sources with optical bandwidths of 2–3 nm [11,12]. Coding was achieved by making use of the grating-lens pulse shaper previously developed for high-resolution pulse shaping and waveform synthesis of coherent femtosecond pulses [13–15]. Binjrajka et al. [16] have subsequently demonstrated coherence coding over a broader bandwidth ($\sim$ 50 nm) centered in the 1.55 μm optical communication band using an EDFA amplified spontaneous emission light source. Their experiments utilized an electronically programmable pulse shaper based on a nematic liquid crystal phase modulator array, which allows high-resolution spectral phase coding under computer control. Simple examples of binary as well as gray-level phase modulation were demonstrated in this work [16].

In the current paper we significantly extend and improve on the work in Ref. [16] by performing coherence coding experiments using spectral phase patterns of substantially higher complexity. In order to achieve successful results, we found that great care was needed to minimize any residual dispersive effects in the pulse shaper. We also found that some of the experimental waveforms were sensitive to the relatively small deviation from the usually assumed linear relation between optical frequency and spatial position at the Fourier plane of the pulse shaper. These factors are of magnified importance in the current experiments due to the increased optical bandwidth compared to our previous experiments using $\sim$ 100 fs optical pulses [14,17]. By properly taking these issues into account, we have now succeeded in experimentally coding the coherence into a number of highly complex waveforms, using both binary and gray-level spectral phase coding. All the results are in excellent agreement with theoretical simulations. We also present spectral interferometry measurements of phase coded incoherent light. Although spectral interferometry is commonly used for pulse characterization by the ultrafast optical community [19,20,22], to our knowledge our measurements mark its first application to characterization of coded incoherent light.

This paper is organized as following. Section 2 gives the theoretical underpinnings and also describes the results in the absence of coding. Section 3 describes experiments in which binary phase sequences are applied to the spectrum of an incoherent ASE light source, resulting in tailored field cross-correlation functions which are in excellent agreement with the simulated results. Also in Section 3, spectral interferometry measurements of such binary code sequences are presented. In Section 4, we successfully implemented complicated gray-level spectral phase coding of incoherent light using quadratic-residue sequences. The generation of coherence functions consisting of trains of coherence peaks was also achieved by applying periodic gray-level phase coding. Complete dispersion compensation of broadband incoherent light using a programmable pulse shaper is also reported. In Section 5, we discuss the errors arising from the usual approximation of a linear spatial dispersion of optical frequency components in the pulse shaper Fourier plane. We report experiments and calculations determining the exact spatial dispersion relation. By using this exact relation, we demonstrate the ability to remove distortion arising when the linear approximation is used.

2. Experimental setup and system alignment

The experimental setup we used is similar to that in Ref. [16] and is shown in Fig. 1. An EDFA pumped by a 980 nm diode laser acts as an ASE source, which is temporally incoherent (strictly speaking, temporally partial incoherent) and which provides an input power of 3 mW to the apparatus. The spectrum spans roughly 50 nm, as seen in Fig. 2(a). The setup is basically a Mach–Zehnder interferometer. In the reference arm, a computer controlled translation stage with a 0.1 μm step size offers adjustable delays. A grating-lens pulse shaper is set in the signal arm. The pulse shaper consists of a pair of gratings, a pair of lenses and a spatial modulation element. The first grating diffracts the frequency components of an input beam to different diffraction angles. These frequency components are then collimated by the first lens to be parallel. A spatial modulation element, such as a mask or a liquid crystal modulator array (LCM), is set in the center of the Fourier plane, which is called a mask plane, to modulate the amplitude or phase, or both,
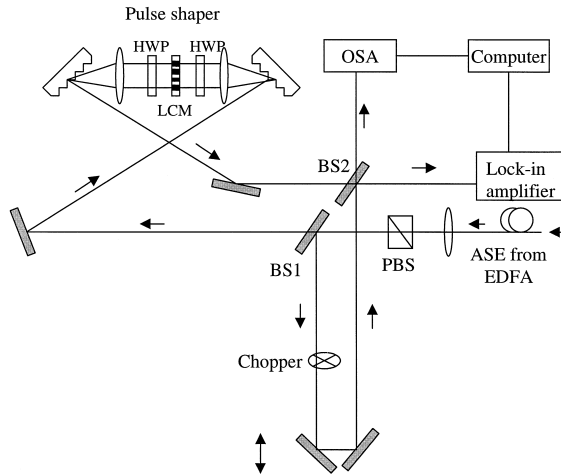
Fig. 1. Experimental setup for phase coding. PBS: Polarizing beam splitter. BS: Beam splitter. LCM: Liquid crystal modulator. HWP: Half-wave plate. OSA: Optical spectrum analyzer. ASE: Amplified spontaneous emission. EDFA: Erbium-doped fiber amplifier.

of each frequency component. In the current experiments we employed only spectral phase modulation. The second lens and grating perform an inverse operation so that all these spatially distributed frequency components are recombined to produce the output beam. In the shaping of coherent femtosecond pulses, the waveform of the output beam is determined by the Fourier transform of the spatial masking function placed onto the spectrum of the input beam [14]. In the current experiments using incoherent light, it is the electric field cross-correlation function between shaped and unshaped light that is tailored according to the Fourier transform of the masking function. To use the gratings in the pulse shaper with maximum diffraction efficiency, a polarizing beam splitter is set at the front of the first beam splitter so that the incident beam to the pulse shaper has the polarization perpendicular to the direction of the grating grooves. Since our LCM requires an input beam with vertical polarization, a half-wave plate is placed before the LCM. A second half-wave plate is put behind the LCM to rotate the polarization of the beam back to horizontal.

In constructing a pulse shaper to accommodate 50 nm bandwidth centered at 1545 nm in the 12.8 mm-wide LCM window, we used a pair of 830 line/mm gratings and a pair of 146 mm focal-length

lenses. The incident angle is $\theta_i \approx 22.6°$ and the diffraction angle is $\theta_{d0} \approx 63.9°$ for the center wavelength. Within a linear approximation, the frequency spatial distribution on the Fourier plane is $d\nu/dx \approx 0.456$ THz/mm.

In Fig. 1, the output of the Mach–Zehnder interferometer can be written as

$$e_{out}(t) = \frac{1}{2} e_{in}(t) \otimes h(t) + \frac{1}{2} e_{in}(t - \tau), \qquad (1)$$

where $e_{in}(t)$ is the complex amplitude of the input light field, $h(t)$ is the response function of the pulse shaper with LCM, τ is the time delay offered by the reference arm, and $\otimes$ is convolution. The detected power can be written as

$$P_{out}(\tau) = \int |e_{in}(t) \otimes h(t)|^2 dt + \int |e_{in}(t - \tau)|^2 dt$$
$$+ \left\{ \int e_{in}(t) \otimes h(t) e_{in}^*(t - \tau) dt \right.$$
$$\left. + \int (c \cdot c) dt \right\}. \qquad (2)$$

The first two terms are DC terms that can be omitted from the measurement. The last two terms corre-
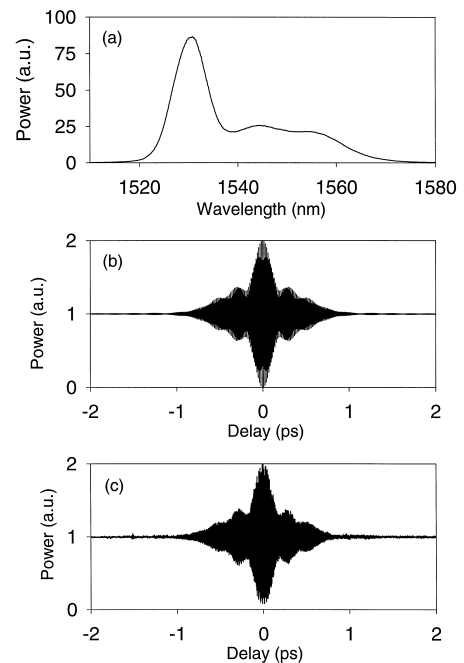

Fig. 2. An incoherent ASE light source: (a) power spectrum; (b) Theoretical field auto-correlation function; and (c) experimental field auto-correlation function.

spond to the interference of the two fields, as a function of the delay between the two arms. When phase coding is performed, the time average of the interference term in Eq. (2) gives the cross-correlation of the two fields from the two arms

$$\Gamma_{\mathrm{cro}}(\tau) \approx \langle e_{\mathrm{in}}(t) \otimes h(t) e_{\mathrm{in}}^*(t - \tau) \rangle, \qquad (3)$$

which can be measured and recorded by a lock-in amplifier. The Fourier transform of Eq. (3) gives the power spectrum representation of the cross-correlation between the reference and the signal fields

$$\mathscr{F}\{\Gamma_{\mathrm{cro}}(\tau)\} = H(\omega)|E(\omega)|^2, \qquad (4)$$

where $H(\omega) = \mathscr{F}\{h(t)\}$. In the case of spectral phase modulation, $H(\omega) = e^{j\phi(\omega)}$.

The power spectrum of the output beam, which is recorded by an optical spectrum analyzer (OSA), is the spectral interferometry signal

$$|E_{\mathrm{out}}(\omega)|^2 = \frac{1}{2}|E_{\mathrm{in}}(\omega)|^2\{1 + \cos[\phi(\omega) + \omega\tau]\}. \qquad (5)$$

The argument of the cosine in the interference term is the phase difference between the two arms. For a fixed τ, the oscillation period of the interference fringes is $2\pi/\tau$. In Eq. (5) we have assumed pure spectral phase modulation, where $\phi(\omega)$ is the phase modulation function applied by an LCM. From an analysis of the spectral interferometry signal of the two output beams from the MZ interferometer, we can extract the phase information carried by the signal beam [21,22].

From Eqs. (3) and (4) we see that when there is no shaping, i.e. $h(t) = \delta(t)$ and $H(\omega) = 1$, we get the field auto-correlation

$$\Gamma_{\mathrm{aut}}(\tau) \approx \langle e_{\mathrm{in}}(t) e_{\mathrm{in}}^*(t - \tau) \rangle, \qquad (6)$$

which is Fourier transform of power spectrum of the input field.

In the current experiments, great care was taken to achieve nearly dispersion free alignment of the pulse shaper. Ideally the completely symmetrical 4F pulse shaper configuration is completely dispersion-free and the output signal from the pulse-shaper is the exactly same as the input [13,23]. However, in practice several factors can disturb this condition. For example, slight misalignments of the two gratings [24,25] and lenses [26] result in the significant

high-order dispersions, which distort the output signal. In our current experiments, we have meticulously adjusted the alignment of the gratings using the following procedures. First, we directed a He–Ne laser, which was set to propagate parallel to the optical table, onto each grating and adjusted the grating orientation to ensure that the diffracted beams corresponding to two different diffraction orders had the same height as the incident beam at a position far from the grating. This ensured that the orientations of the gratings and the grating grooves were perpendicular to the plane of the optical table. Second, we directed a tunable erbium-doped fiber laser onto the first grating and rotated the second grating carefully to ensure that the output beam at a position far from the second grating did not move when the input wavelength was turned over a 40 nm range around 1545 nm. This procedure ensures that the incidence angle on the first grating and the diffraction angle on the second grating are equal. We also ensured that the two lenses were carefully centered in the beam and untilted with respect to the direction of the beam propagation. These efforts minimized any dispersion from the pulse shaper.

Fig. 2(a) shows the power spectrum of the input ASE source from an EDFA. Fig. 2(b) and Fig. 2(c) are the simulation results and the experimental data of the field auto-correlation of this input ASE light, respectively. The spectrum spans roughly 50 nm, as seen in Fig. 2(a), which leads to the narrow center peak of duration approximately 0.2 ps in the field auto-correlation. The narrow peak in the ASE power spectrum around 1530 nm leads to an overall duration of roughly 1 ps of the ASE auto-correlation. The excellent agreement between the simulated and experimental auto-correlations indicates that close-to-dispersion-free alignment of the pulse shaper has been achieved, which is necessary for precise phase coding of the incoherent light source.

3. Binary phase coding

In these experiments, a series of different bipolar phase sequences were applied onto the ASE spectrum. Three sets of data are shown in Fig. 3. The top and bottom rows are the computer simulations and
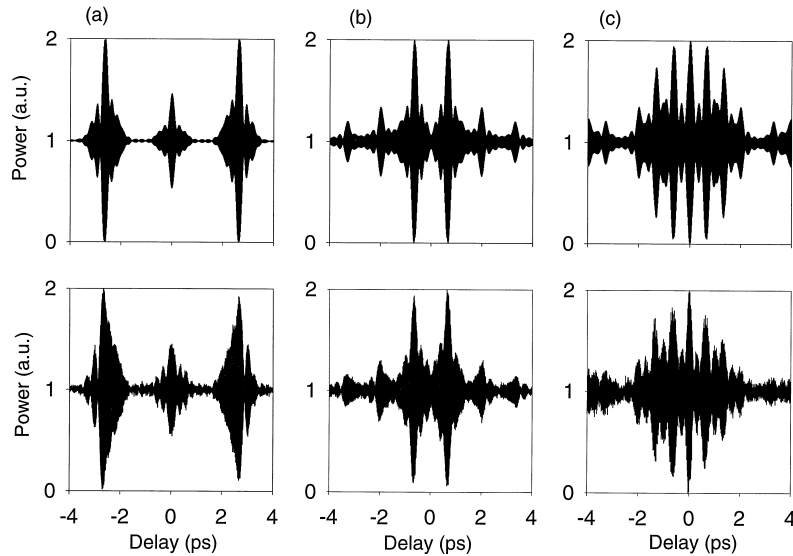
Fig. 3. Binary phase coding. The top and bottom rows are the simulated and experimental field cross-correlations of the coded pulses, respectively. In column (a) the phase code sequence is a cycle of 3 pixels at 0 and 5 pixels at π repeated 16 times. In column (b) the phase sequence is a cycle of 16 pixels at 0 and 16 pixels at π repeated 4 times. In column (c) the phase sequence is a cycle of 24 pixels at 0 and 8 pixels at π repeated 4 times.

experimental measurements of the field cross-correlation functions, respectively. In Fig. 3(a), the phase code sequence is a cycle of 3 LCM pixels set for 0 phase and 5 pixels set for π phase, repeated a total of 16 times to fill the 128 LCM pixels. In Fig. 3(b) the phase code consists of repetition of a cycle of 16 pixels at 0 phase and 16 pixels at π. In Fig. 3(c), the phase code consists of repetition of a cycle of 24 pixels set for 0 phase and 8 pixels set for π. The good agreement between simulations and experimental results demonstrates both a nearly dispersion-free configuration and a highly precise spatial phase modulation implemented by the LCM. The slight difference between the simulated and experimental traces in Fig. 3(a) may result from the assumption of a linear spread of frequency components in the pulse shaper Fourier plane. This point will be discussed in Section 5.

We also used spectral interferometry to measure the spectral phase codes applied by the LCM onto incoherent light. Two examples of restored phase codes, extracted from spectral interferometry data [22], are shown in Fig. 4. Both measurements are consistent with the applied phase codes programmed onto the LCM. These results further demonstrate the
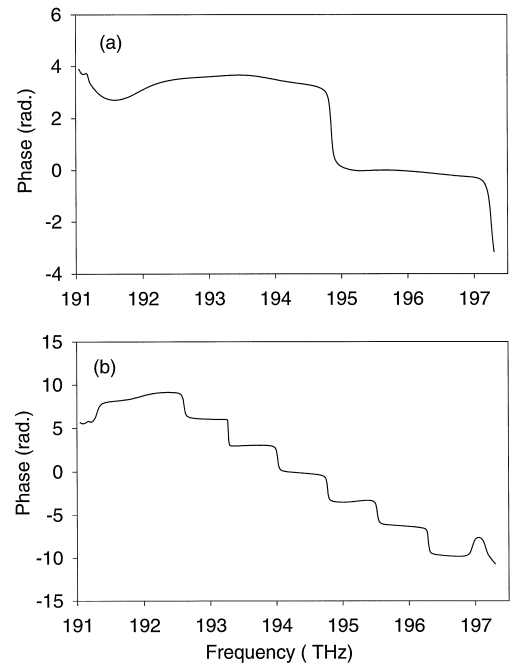

Fig. 4. Binary phase sequences recovered from spectral interferometry data. In (a) the applied phase sequence consists of 64 pixels at 0 and the rest 64 pixels at π. In (b) the applied phase sequence consists of four repetitions of 16 pixels at 0 and 16 pixels at π.

validity of spectral phase coding onto an incoherent light source.

We see from the above binary phase coding experiments that output field cross-correlation functions of the coded incoherent light with the reference beam have more complicated shapes than those that would be observed in pulse shaping experiments with coherent femtosecond pulses. This results from the use of an ASE source with a structured broadband spectrum and a relatively complex auto-correlation, which is one reason for a high sensitivity to residual dispersion in the pulse shaper. Therefore, to get precisely controlled coding results with incoherent light, it may be preferable to have a source with a broad and smooth spectrum. However, on the other hand, high sensitivity and complex cross-correlation functions may fit the requirement of high security for communication networks, e.g. for the military and banking communities.

4. Complicated gray-level spectral phase modulation

Since a commercial LCM with 128 elements offers 4096 voltage drive levels to control the phase change in the range of 0–2.5π from one pixel to the next, the pulse shaper with a LCM makes it available to perform more complicated gray-level phase modulation or phase coding. Here we demonstrate three examples of gray-level spectral phase modulation of incoherent light, namely: (a) spectral phase coding using quadratic-residue codes; (b) periodic spectral phase modulation resulting in a multiply peaked coherence function; and (c) complete dispersion compensation.

4.1. Spectral phase coding using quadratic-residue sequences

A quadratic-residue sequence is defined [27] as

$$r_n = e^{i2\pi n^2/p}, \quad n = 0, 1, \ldots, p-1, \quad (7)$$

where p is a prime. This quadratic-residue sequence has the cross- and auto-correlation properties

$$C_k = \sum_{n=0}^{p-1} r_n r_{n+k}^* = e^{-i2\pi k^2/p} \sum_{n=0}^{p-1} e^{-i4\pi nk/p}$$

$$C_k = \begin{cases} 0 & \text{for } k \neq 0 \ (\text{mod } p), \\ p & \text{for } k = 0 \ (\text{mod } p). \end{cases} \quad (8)$$

These properties make the quadratic-residue sequences attractive codes for the spectral phase coding in optical CDMA communications [28–30] to minimize interference. These codes were previously used in CDMA wireless communications [26].

For applying the quadratic-residue sequences to spectral phase coding, we can write phase modulation function as

$$\phi_n(\nu) = \frac{2\pi n^2}{p}, \quad n = 0, 1, 2, \ldots, p-1, \quad (9)$$

where p is a prime. Then the response function of a LCM can be expressed as

$$H_n(\nu) = e^{i\phi_n(\nu)} = e^{i2\pi n^2/p}, \quad n = 0, 1, \ldots, p-1. \quad (10)$$

The pixels of an LCM are equally spaced. Within a linear approximation, we assume that the frequency change from one pixel to the next is a constant. Note that since p is a prime and one pixel is the minimum unit, we can not employ a quadratic-residue sequence with p elements to cover the entire 128 pixels exactly. What we did is to take $p < 128$, let each $[128/p]$ pixels share the same phase value, and set the extra pixels to 0 phase. For an example of $p = 11$, each $[128/11] = 11$ pixels correspond to one 'chip' with the phase value $2\pi n^2/p$. The extra 7 pixels are set to 0 phase. Because the liquid crystal array is restricted to the maximum phase shift of 2.5π, all phase shifts bigger than 2π were folded back into the range of $0 \sim 2\pi$. A computer program converted derived phase values to the corresponding voltages, which were applied to the LCM array through an electronic controller.

Fig. 5 shows two sets of simulated and experimental results for quadratic-residue phase coding of the incoherent ASE source. Fig. 5(a) and Fig. 5(b) are the results for $p = 11$ and $p = 31$, respectively. The top row shows the simulation results, while the
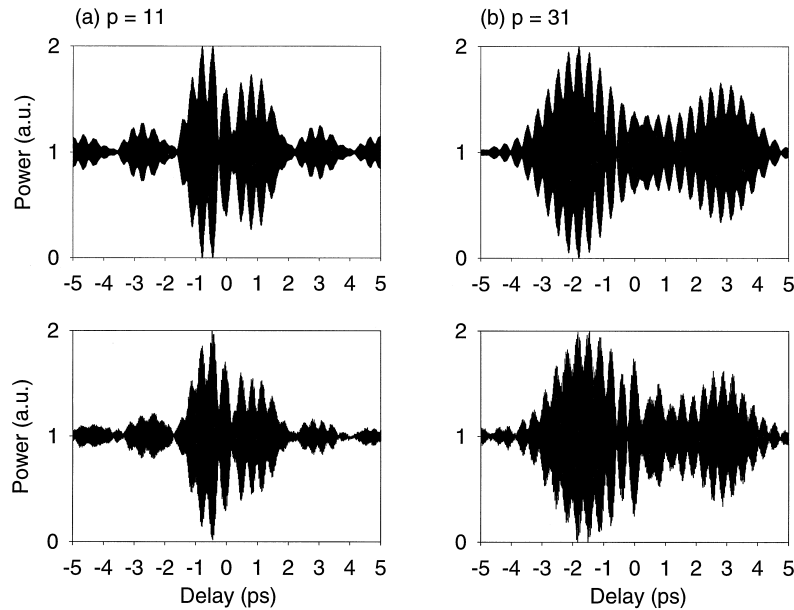
Fig. 5. Quadratic-residue phase coding. The top and bottom rows are the simulated and the experimental field cross-correlations, respectively. Column (a) is for the phase sequence with $p = 11$. Column (b) is for the phase sequence with $p = 31$.

bottom row shows the experimental field cross-correlation data in the time domain. The excellent agreement between the theoretical simulations and the experimental data gives further indication of the fidelity of our spectral phase coding technique and the ability to precisely control phase with multiple gray-levels.

4.2. Periodic gray-level spectral phase modulation

Weiner and co-workers [17,31] demonstrated the generation of high-quality pulse trains by using periodic binary spectral phase filtering in coherent femtosecond pulse shaping experiments. Here we implemented periodic gray-level spectral phase coding on incoherent light for the first time. We let each value of a quadratic-residue sequence be assigned to a single LCM pixel. Still within the approximation of linear spectral dispersion, each pixel corresponds to $d\nu = 45.6$ GHz. For a quadratic-residue sequence of length p (p is a prime), the LCM phase repeats every p pixels, resulting in a frequency periodicity $\Delta\nu = p \times d\nu$. The resulting coherence function consists of a series of peaks separated by delay $\Delta\nu^{-1}$. As an example of $p = 7$, the quadratic phase code

$\{0, 1, 4, 9, 16, 25, 36\} \cdot 2\pi/7$, or equivalently $\{0, 1, 4, 2, 2, 4, 1\} \cdot 2\pi/7$, is periodically applied to the spectrum. Then, the frequency periodicity is $\Delta\nu = 0.32$ THz. We implemented the theoretical simulations and experimental demonstrations of phase coding based on the periodic quadratic-residue sequences. The results for $p = 7$ and $p = 11$ are shown in Fig. 6(a) and Fig. 6(b), respectively. From the simulations we observe that the resulting pulse trains consist of a series of isolated peaks, the shapes and durations of which are the same as the field auto-correlation of the unshaped light. We noted that for the case of $p = 11$, the frequency periodicity is $\Delta\nu = 0.5$ THz. The time separation between the two neighboring peaks is $\Delta t = 2$ ps, which is not much longer than the ~ 1 ps correlation time of the incoherent ASE light (see Fig. 2(a)). Therefore, periodic phase coding by quadratic-residue sequences of $p > 11$ will cause the adjacent peaks in a train to overlap and interfere with one another, leading to more complicated waveforms. In Fig. 6, the experimental traces match the theoretical ones qualitatively. The asymmetric waveform distortion of some of the peaks may again result from the effect of nonlinear frequency mapping in the mask plane, which is not
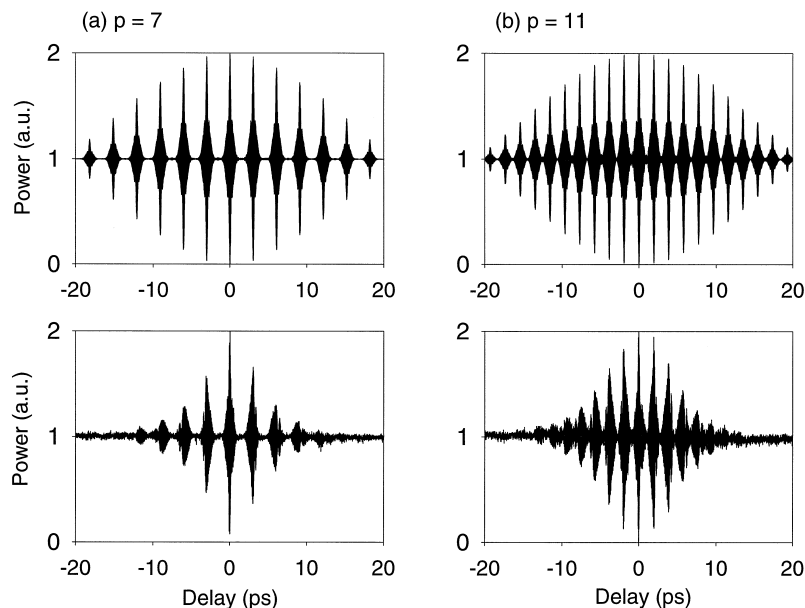
Fig. 6. Spectral phase coding based on periodic quadratic-residue sequences. The top and bottom rows are the simulated and the experimental field cross-correlations, respectively. Column (a) is for the quadratic-residue sequence with $p = 7$ and frequency periodicity $\Delta \nu = 0.32$ THz. Column (b) is for $p = 11$ and $\Delta \nu = 0.5$ THz.

taken into account in these experiments. The amplitude decrease in the wings of the experimental traces may arise from the finite spectral resolution of the pulse shaper apparatus [31].

4.3. Complete dispersion compensation

Gray-level spectral phase modulation can also be used to correct dispersion experienced by broadband incoherent light. Phase correction of coherent femtosecond pulses using a programmable pulse shaper was previously demonstrated in Refs. [17,32], with application to cubic phase compensation for optical fiber transmission [33], and cubic and quadratic dispersion compensation for chirped pulse amplifiers [34]. In the case of incoherent light, the field correlation function will not change if both reference and signal pulses experience identical dispersions. However, the field cross-correlation will be distorted if only the signal experiences dispersion, or if both of the beams experience different amounts of dispersion. We demonstrate correction of such distortion here for the first time.

Two examples of distortion caused by signal dispersion are presented in Fig. 7(a) and Fig. 7(b), respectively. Fig. 7(a) shows the field cross-correlation of a distorted waveform caused by the second lens being rotated by about 2° around the vertical axis, which may result in the third-order dispersion mainly [26]. Fig. 7(b) shows another example of waveform distortion caused by the second grating shifting away from the focal plane of the second lens by ∼ 0.24 mm in our pulse shaper, which mainly causes second- and third-order dispersions [35]. Here we demonstrate complete dispersion compensation for the example of the waveform distortion shown in Fig. 7(b), without making any assumption about which orders of dispersion are present. First, using an optical spectral analyzer (OSA) and setting the time delay between the two arms to $\tau > T$, where T is the correlation time of the incoherent light source, we measured the spectral interferometry signal of the recombined output beams from the Mach–Zehnder interferometer with no applied phase modulation. Second, through an analysis of the spectral interferometry data using a technique similar to the one in
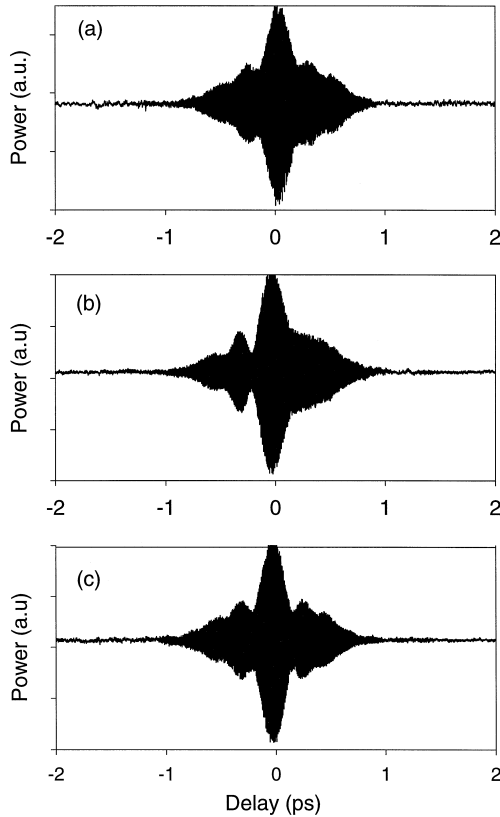
Fig. 7. Waveform distortion caused by dispersion and dispersion compensation by using a programmable LCM: (a) field cross-correlation of a distorted waveform resulting from a small lens tilt; (b) field cross-correlation of a distorted waveform resulting from a small grating shift; (c) field cross-correlation of the waveform in (b) compensated by a proper phase modulation applied by a programmable LCM.

Ref. [22], we extracted the phase information $\phi(\omega)$ of the distorted output field from the pulse shaper. Third, by programming the LCM, a phase modulation function $\phi'(\omega) = -\phi(\omega)$ was applied onto the input beam spectrum, so that the residual dispersion of the pulse shaper was compensated. Fig. 7(c) shows the field cross-correlation function of the compensated incoherent light as a function of delay. The good symmetry of Fig. 7(c) indicates that the desired close-to-dispersion-free condition has been achieved. This technique can be used for precise dispersion compensation with arbitrary phase modulation functions, provided the phase information $\phi(\omega)$ can be obtained and the spectral phase varies sufficiently

slowly that it is adequately sampled by the LCM pixels.

5. Improved phase coding precision by using the exact space-frequency mapping relationship

In the previous phase modulation work using a LCM [16–18], it has usually been assumed for the sake of simplicity that the frequency change from one pixel to the next is a constant. For most experimental conditions this linear approximation works well. However, we know that in reality the frequency components are not linearly dispersed over the mask plane in a pulse shaper. Weiner et al. [14] noted a subtle effect in an experimental power spectrum due to nonlinear spatial dispersion. Efimov et al. [32] numerically simulated the effect of nonlinear spatial dispersion within a pulse shaper for assumed ultra-broad-bandwidth femtosecond pulses, e.g. with 400 nm bandwidths. Recently, Gouvea et al. [36] pointed out that for long wavelengths and very large incident angles on the grating, the linear approximation does not give an accurate enough prediction. In some practical circumstances, programming the LCM assuming linear spatial dispersion will cause significant deviation from the theoretical expectation. We have already noted some waveform distortions, which we assigned to this effect in earlier figures. In the following we report a clear experimental demonstration of waveform distortions due to nonlinear spatial dispersion in programmable time delay experiments implemented by linear spectral phase modulation. We also demonstrate correction of these effects.

Suppose the light field $e(t)$ and $E(\omega)$ are a Fourier transform pair

$$e(t) = \frac{1}{2\pi} \int_{-\infty}^{\infty} E(\omega) e^{i\omega t} d\omega. \tag{11}$$

Then, a linear phase modulation in the frequency domain, $\phi(\omega) = -\omega\tau$, corresponds to a temporal shift in the field without changing the waveform and amplitude.

$$\frac{1}{2\pi} \int_{-\infty}^{\infty} E(\omega) e^{i\phi(\omega)} e^{i\omega t} d\omega$$
$$= \frac{1}{2\pi} \int_{-\infty}^{\infty} E(\omega) e^{i\omega(t-\tau)} d\omega = e(t-\tau). \tag{12}$$
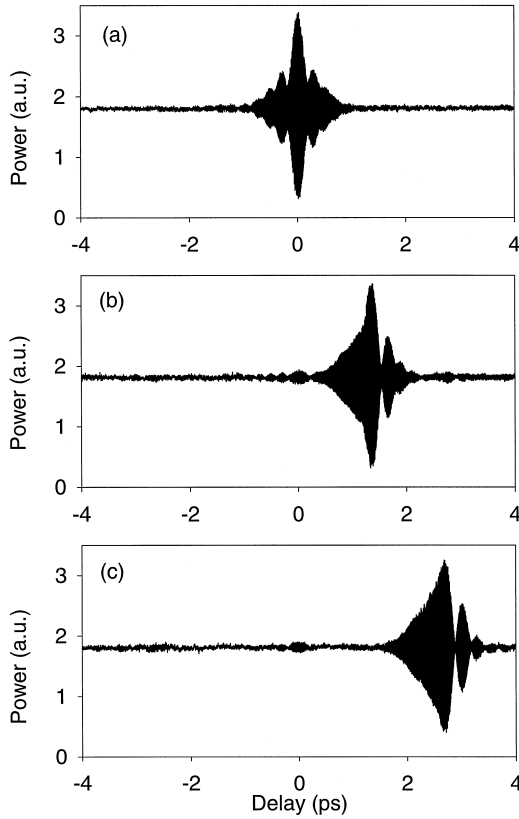
Fig. 8. Time delay by linear spectral phase modulation, assuming linear spatial dispersion of frequency components on the mask plane. In (b) and (c) the phase change per pixel is $1/8\pi$ and $1/4\pi$, respectively. The calculated time shifts are 1.368 ps and 2.735 ps, respectively. Note that vertical scales are the same for all (a)–(c).

We initially performed the experiments to apply a linear spectral phase sweep onto the incoherent light spectrum assuming a linear relation between the pixel position and the frequency change on the mask plane. Fig. 8(a) is the field auto-correlation of the incoherent ASE light without the phase modulation. In Fig. 8(b) and Fig. 8(c), the phase change per pixel is $1/8\pi$ and $1/4\pi$, respectively. For our setup, the bandwidth of the ASE light covered by the total 128 pixels is 46.8 nm (5.85 THz). The calculation by using $\tau = -((d\phi(\omega))/d\omega)$ gives the results $\tau = 1.368$ ps and $\tau = 2.735$ ps, respectively, which are in good agreement with the measured delays in Fig. 8(b) and Fig. 8(c). Note that the amplitude of the shifted waveforms is not reduced as in the previous

experiments [16], where less attention was paid to the pulse shaper alignment. However, there is obvious asymmetry and distortion in the shifted waveforms, which is not present in the unshifted case. The main source of this distortion is the effect of nonlinear spatial dispersion.

In order to correct this effect, we need to determine the exact relation between the frequency distribution in the mask plane and the position of LCM pixels. For the theoretical calculation, two equations are used. One is the first-order grating equation

$$\sin\theta_d + \sin\theta_i = \frac{\lambda}{d}, \qquad (13)$$

where the incident angle θ_i is fixed, θ_d is the diffraction angle and d is the grating constant. The other one is the equation:

$$\tan(\theta_d - \theta_{d0}) = \frac{x}{F}, \qquad (14)$$

where θ_{d0} is the diffraction angle of the center wavelength λ_0, F is the focal length of the lens and x is the lateral displacement of a particular frequency component away from the optical axis, as seen in Fig. 9.

On the other hand, we can find the real frequency distribution on the LCM pixels experimentally. Using the LCM and considering the measurement resolution, a phase sequence of $00\pi\pi00\pi\pi00\pi\pi\ldots$ repeating over the full 128 pixels was applied onto the spectrum of the incoherent light. The power spectrum of this coded incoherent light is shown in Fig. 10. We know that every $0 \rightarrow \pi$ jump in phase
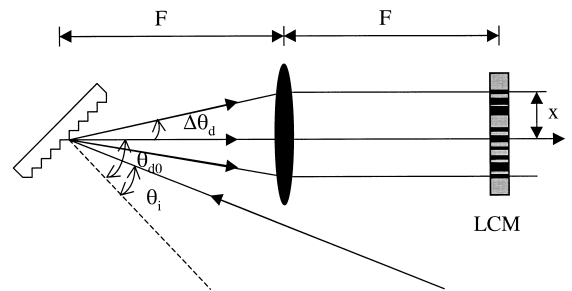

Fig. 9. Configuration of frequency components spreading over the window of a LCM in a pulse shaper. θ_i is the incident angle and θ_{d0} is the diffraction angle of the center wavelength λ_0. $\Delta\theta_d = \Delta\theta_d - \theta_{d0}$. F is the focal length of the lens. LCM: Liquid crystal modulator.
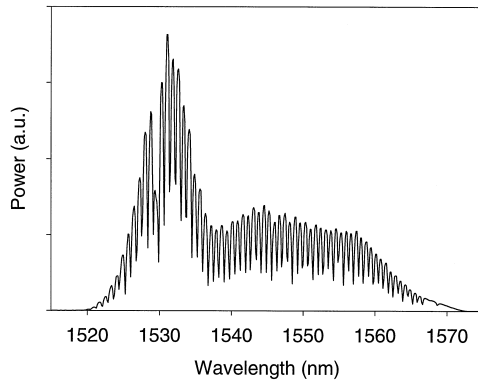
Fig. 10. Power spectrum of ASE light coded by the phase sequence $00\pi\pi00\pi\pi00\pi\pi\ldots$ repeating over 128 pixels. The valley bottoms correspond to the positions where phase jumps $0 \rightarrow \pi$ occur. Note that the deep hole at $\lambda \approx 1530$ nm arises from a bad pixel.

leads to a notch in the power spectrum due to diffraction of those frequency components impinging on the $0 \rightarrow \pi$ transition [37]. Therefore, by recording the positions of the minimum values in the power spectrum data of Fig. 10, we obtained the one-to-one mapping relation of frequency vs. position of the individual pixels. Note that these minima correspond to the positions of pixel edges. The theoretical estimate and the experimental measurement of frequency vs. pixel position match each other quite well. Note that in Fig. 10 a bad LCM pixel at $\lambda \sim 1.53$ μm results in a bigger drop, but it does not seriously effect our measurement. From Fig. 11(a) we see that the measurement of frequency vs. pixel position clearly deviates from the assumed linear approximation. Fig. 11(b) shows the results of subtracting the linear curve from the data. The observed deviation from the linear approximation is in close agreement with the theoretical prediction. The oscillation at the left side of the experimental trace in Fig. 11(b) is assigned to fluctuations in the measurements. The maximum frequency deviation of ~ 176 GHz at the two ends of the LCM window is roughly four times the 45.6 GHz average frequency range covered by one pixel.

By using this exact nonlinear mapping function between frequency and pixel position, i.e., $\nu_n = \nu(n)$, where n is the pixel number, we can perform the programmable spectral phase modulation more accu-

rately. As an application example, now we repeat our programmable time delay experiments on incoherent light and employ a LCM to apply a *real* linear phase modulation

$$\phi_n(\nu) = A(\nu_n - \nu_1) \quad n = 1, 2, \ldots, 128 \qquad (15)$$

on the nth pixel. Here, A is a constant, ν_n is the frequency corresponding to the nth pixel and ν_1 is a reference frequency. For a specified A, we need to convert the various phase values in Eq. (15) into the corresponding drive voltages, which are then applied to the LCM array. In Fig. 12(b) and Fig. 12(c), the total phase sweeps over 128 pixels are $8 \times 2\pi$ and $16 \times 2\pi$, respectively. The experimental delay times are 1.37 ps and 2.74 ps, respectively, which are in excellent agreement with the theoretical calculation. The waveform amplitude does not change at all, as we expected. From Fig. 12(a)–Fig. 12(c) we also see that before and after the linear phase modulation, the
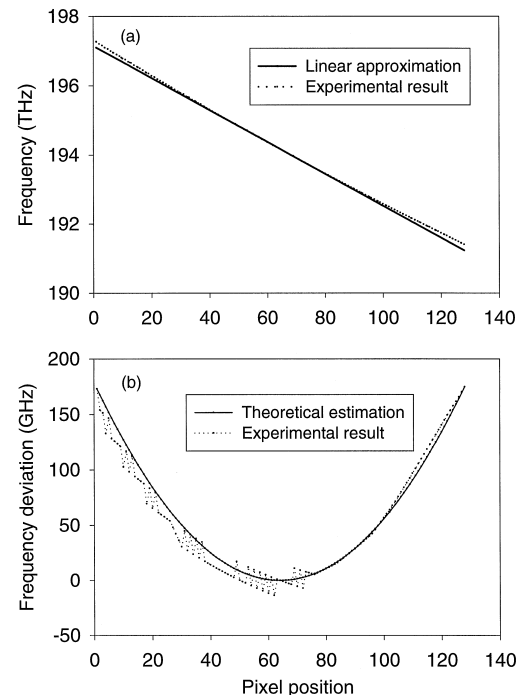

Fig. 11. Nonlinearity of spatial frequency distribution: (a) the measured frequency vs. pixel position curve clearly deviates from the linear approximation; and (b) deviations of the theoretical and experimental frequency vs. the pixel position traces from a straight line, respectively.
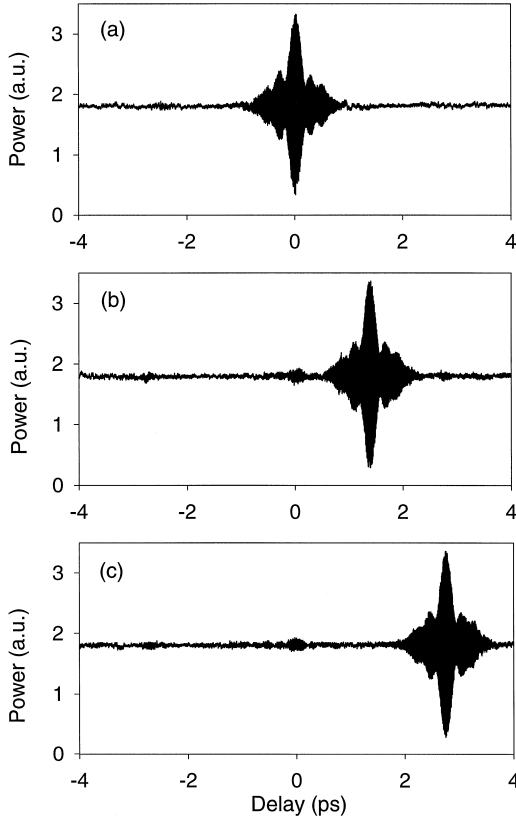
Fig. 12. Time delay by linear phase modulation based on exact nonlinear relation of the frequency vs. the pixel position. In (b) and (c) the total phase sweeps over 128 pixels are 8π and 16π, respectively. The calculated time shifts are 1.368 ps and 2.735 ps, respectively. Note that vertical scales are the same for all (a)–(c).

waveforms basically remain the same, showing a great improvement compared with Fig. 8(a)–Fig. 8(c).

In general, the effect of the nonlinear frequency vs. pixel mapping depends on the exact waveform under consideration. However, our method of compensating for this nonlinear mapping, demonstrated above, can be applied to any waveform, including binary and gray-level spectral phase modulation, and spectral amplitude modulation as well.

We now estimate the effect of nonlinear spatial dispersion under different experimental conditions. In Ref. [31] expressions for high-order wavelength deviations, $(d\lambda/dx)_{\lambda_0}$, $(d^2\lambda/dx^2)_{\lambda_0}$ and $(d^3\lambda/dx^3)_{\lambda_0}$, were given, where λ_0 is the center wave-

length of the input beam. In Refs. [18,35], the spatial dispersion is approximately written as

$$x \approx F\left[\left(\frac{\partial\theta}{\partial\omega}\right)_{\omega_0}(\omega - \omega_0) + \frac{1}{2}\left(\frac{\partial^2\theta}{\partial\omega^2}\right)_{\omega_0}(\omega - \omega_0)^2\right], \quad (16)$$

where expressions for $(\partial\theta/\partial\omega)_{\omega_0}$ and $(\partial^2\theta/\partial\omega^2)_{\omega_0}$ are given and $\omega_0 = 2\pi c/\lambda_0$. Because pulse shaping is most conveniently analyzed in the frequency domain and the LCM pixels are equally spaced and fixed, we prefer to use the Taylor series expansion of frequency ν vs. location x

$$\nu(x) = \nu_0 + \left(\frac{\partial\nu}{\partial x}\right)_{x_0}x + \frac{1}{2}\left(\frac{\partial^2\nu}{\partial x^2}\right)_{x_0}x^2 + \frac{1}{6}\left(\frac{\partial^3\nu}{\partial x^3}\right)_{x_0}x^3 + \cdots, \quad (17)$$

where $x_0 = 0$ corresponds the location of the center frequency in Fig. 9. From Eqs. (13) and (14) the partial derivatives $\partial^n\nu/\partial x^n$ can be derived with the following results:

$$\left(\frac{\partial\nu}{\partial x}\right)_{x_0} = -\frac{d\cos\theta_{d_0}}{Fc}\nu_0^2,$$

$$\left(\frac{\partial^2\nu}{\partial x^2}\right)_{x_0} = \frac{d^2\nu_0^3}{F^2c^2}\left(\frac{c}{d\nu_0}\sin\theta_{d_0} + 2\cos^2\theta_{d_0}\right),$$

$$\left(\frac{\partial^3\nu}{\partial x^3}\right)_{x_0} = \frac{d\nu_0^2}{cF^3}\left(3\cos\theta_{d_0} - \frac{d\nu_0}{c}\sin 2\theta_{d_0} - \frac{6d^2\nu_0^2}{c^2}\cos^3\theta_{d_0}\right). \quad (18)$$

The absolute value of the ratio of the second-order term to the first-order term in Eq. (17) at a specific position x is

$$R = \frac{x}{2F}\left(\tan\theta_{d_0} + \frac{2d}{\lambda_0}\cos\theta_{d_0}\right). \quad (19)$$

In the case that the bandwidth of the input light is spread to an aperture matching or exceeding the LCM window L, then $x_{max} = 1/2\ L$. Then,

$$R_{max} = \frac{L}{4F}\left(\tan\theta_{d_0} + \frac{2d}{\lambda_0}\cos\theta_{d_0}\right), \quad (20)$$

which is determined by the setup parameters and the center wavelength of the input light. This is a precise expression for R_{max}. When $\theta_{d0} \gg 45°$ or $d/\lambda_0 > 1$, the nonlinearity of the spatial frequency dispersion can impose a noticeable effect on the system performance, especially for a complex light waveform like our case.

Usually, when designing a pulse shaper, the mask aperture size should accommodate the desired bandwidth of the input light source. To estimate R_{max} by utilizing the available bandwidth, we can take the approximation (linear)

$$x_{max} = (x - x_0)_{max} \approx \frac{(\nu - \nu_0)_{max}}{\left(\frac{\partial \nu}{\partial x}\right)_{x_0}} = \frac{\Delta \nu_{max}}{\left(\frac{\partial \nu}{\partial x}\right)_{x_0}}.$$ (21)

Substituting Eq. (21) and Eq. (18) in Eq. (19), we get

$$R_{max} \approx \frac{\Delta \nu_{max}}{\nu_0} \left(1 + \frac{1}{2} \frac{\lambda_0 \sin\theta_{d0}}{d \cos^2\theta_{d0}} \right).$$ (22)

Note that F drops out and the total bandwidth passed by the pulse shaper aperture of $2\Delta x_{max}$ is $2\Delta \nu_{max}$. Therefore, R_{max} becomes important for large fractional bandwidth $\Delta \nu_{max}/\nu_0$, as well as when λ_0/d increases or θ_{d0} becomes large.

Since the ratio of the third-order term to the first-term in Eq. (17) is less than 10^{-3} in our experiments, here we ignore the effect of terms higher than the second-order.

For our experimental parameters, we get $R_{max} \approx 6.0\%$ by using either Eq. (20) or Eq. (22). The actual bandwidth accommodated in our LCM window is about 5.85 THz. Therefore, the deviation at the edges of the LCM window from the assumed linear spreading is

$$\Delta \nu \approx \frac{5.85}{2} \text{THz} \times R_{max} \approx 175.5 \text{ GHz},$$ (23)

which matches the experimental observation in Fig. 11 quite well. Since the average frequency segment covered by one pixel is about 45.6 GHz, the frequency deviation at the edges of the LCM aperture is equivalent to ~ 4 pixels, which can cause significant effects on the observed waveforms.

The setups used in Refs. [14,17] have $\lambda_0 = 0.62$ μm, $F = 150$ mm and $\theta_{d0} = 35°$. For $d = 1/1700$

mm and $L = 2.5$ mm in Ref. [14], we got $R_{max} \approx 0.94\%$ by using Eq. (20). For $d = 1/1800$ and $L = 5.12$ mm in Ref. [17] we got $R_{max} \approx 1.85\%$. For the experiments in Ref. [17] with FWHM bandwidth ~ 10 nm at the center wavelength $\lambda_0 = 0.62$ μm, the $1/e^2$ power bandwidth accommodated by the LCM window is about 13.26 THz. By using Eq. (22) we got $R_{max} \approx 1.99\%$. These values of R_{max} are 3–6 times less than our setup. This explains why our setup is more sensitive to the variation in $d\nu/dx$. (The use of an incoherent ASE source with a complex waveform is also a factor.) Note that in our current experiments, $(\Delta \nu/\nu_0) \approx 0.015$ and $(\lambda_0 \sin\theta_d)/(2d \cos^2\theta_d) \approx 2.976$. In Ref. [14], $(\Delta \nu/\nu_0) \approx 0.0137$ and $(\lambda_0 \sin\theta_d)/(2d \cos^2\theta_d) \approx 0.451$. The fractional bandwidths $\Delta \nu/\nu_0$ are about the same. However, $(\lambda_0 \sin\theta_d)/(2d \cos^2\theta_d)$ is six times larger in the current experiments, which results in the larger value of R_{max}.

6. Conclusion

In this paper, we have experimentally demonstrated high fidelity binary and gray-level spectral phase coding of an incoherent ASE light source by using a pulse shaper and a programmable LCM. The excellent agreement between the theoretical simulations and experimental measurements indicates the high precision of our spectral phase coding techniques. We also considered the effect of nonlinearties in the spatial dispersion and determined the exact mapping between the optical frequency and the pixel location. We showed that by using this exact mapping information, we could improve the precision of our phase-coded waveforms. Finally, we derived expressions useful for estimating the importance of the nonlinearity of the frequency distribution under specified experimental conditions.

Acknowledgements

References

[1] R.D.T. Lauder, J.M. Badcock, W.T. Holloway, D.D. Sampton, IEEE Photon. Technol. Lett. 10 (1998) 294.

[2] A.J. Keating, D.D. Sampson, J. Lightwave Technol. 15 (1997) 53.

[3] D. Zaccarin, M. Kavehrad, IEEE Photon. Technol. Lett. 4 (1993) 479.

[4] R.A. Griffin, D.D. Sampson, D.A. Jackson, J. Lightwave Technol. 3 (1995) 1826.

[5] D.D. Sampson, G.J. Pendock, R.A. Griffin, Fiber Integr. Opt. 16 (1997) 129.

[6] E.D. Smith, P.T. Gough, D.P. Taylor, Electron. Lett. 31 (1995) 1469.

[7] L. Nguyen, T. Dennis, B. Aazhang, J.F. Young, J. Lightwave Technol. 15 (1997) 1647.

[8] K.W. Chu, F.M. Dickey, Opt. Eng. 30 (1991) 337.

[9] G.J. Pendock, D.D. Sampson, IEEE Photon. Technol. 7 (1995) 1504.

[10] D.D. Sampson, D.A. Jackson, Opt. Lett. 15 (1990) 585.

[11] R.A. Griffin, D.D. Sampson, D.A. Jackson, IEEE J. Lightwave Technol. 13 (1995) 1826.

[12] H. Sonajalg, A. Debarre, J.-L.L. Gouet, I. Lorgere, P. Tchenio, J. Opt. Soc. Am. B 12 (1995) 1448.

[13] A.M. Weiner, J.P. Heritage, Rev. Phys. Appl. 22 (1987) 1619.

[14] A.M. Weiner, J.P. Heritage, E.M. Kirschner, J. Opt. Soc. Am. B 5 (1988) 1563.

[15] A.M. Weiner, Prog. Quantum Electron. 19 (1995) 161.

[16] V. Binjrajka, C.C. Chang, A.W.R. Emanuel, D.E. Leaird, A.M. Weiner, Opt. Lett. 21 (1996) 1756.

[17] A.M. Weiner, D.E. Leaird, J.P. Patel, J.R. Wullert, IEEE J. Quantum Electron. 28 (1992) 908.

[18] M.M. Wefers, K.A. Nelson, J. Opt. Soc. Am. B 12 (1995) 1343.

[19] E. Tokunaga, A. Terakasa, T. Kobayashi, J. Opt. Soc. Am. B 12 (1995) 753.

[20] X.D. Cao, D.D. Meyerhofer, Opt. Lett. 19 (1994) 1837.

[21] K. Naganuma, K. Mogi, H. Yamada, Opt. Lett. 15 (1990) 393.

[22] L. Lepetit, G. Cheriaux, M. Joffre, J. Opt. Soc. Am. B 12 (1995) 2467.

[23] O.E. Martinez, J. Quantum Electron. 23 (1987) 59.

[24] K. Osvay, I.N. Ross, Opt. Commun. 105 (1994) 271.

[25] Z. Zhang, T. Yagi, J. Appl. Phys. 77 (1994) 937.

[26] K.C. Chu, J.P. Heritage, R.S. Grant, Opt. Lett. 21 (1996) 1842.

[27] M.R. Schroeder, Number Theory in Science and Communication, Springer-Verlag, Berlin, 1997.

[28] F.R.K. Chung, J.A. Salehi, V.K. Wei, IEEE Trans. Inf. Theory. 35 (1989) 595.

[29] J.A. Salehi, IEEE Trans. Commun. 37 (1989) 824.

[30] H.P. Sardesai, C.-C. Chang, A.M. Weiner, IEEE J. Lightwave Technol. 16 (1998) 1953.

[31] A.M. Weiner, D.E. Leaird, Opt. Lett. 15 (1990) 51.

[32] A. Efimov, C. Schaffer, D.H. Reitze, J. Opt. Soc. Am. B 12 (1995) 1968.

[33] C.-C. Chang, H.P. Sardesai, A.M. Weiner, Opt. Lett. 23 (1998) 283.

[34] A. Efimov, D.H. Reitze, Opt. Lett. 23 (1998) 1612.

[35] M. Stern, J.P. Heritage, E.W. Chase, IEEE J. Quantum Electron. 28 (1992) 2742.

[36] P.M. Gouvea, E.W. Hansen, U.L. Osterberg, D. Healy, Opt. Commun. 147 (1998) 163.

[37] R.N. Thuston, J.P. Heritage, A.M. Weiner, W.J. Tomlinson, IEEE J. Quantum Electron. 22 (1986) 682.